Mechanical properties prediction of blast furnace slag and fly ash-based alkali-activated concrete by machine learning methods

SUN, Beibei; DING, Luchuan; YE, Guang; De SCHUTTER, Geert

DOI
10.1016/j.conbuildmat.2023.133933

Publication date
2023

Document Version
Final published version

Published in
Construction and Building Materials

Construction and Building Materials 409 (2023) 133933

Contents lists available at ScienceDirect

Construction and Building Materials

journal homepage: www.elsevier.com/locate/conbuildmat

Mechanical properties prediction of blast furnace slag and fly ash-based alkali-activated concrete by machine learning methods

Beibei SUN [a], Luchuan DING [c], Guang YE [a,b,*], Geert De SCHUTTER [a,*]

[a] Ghent University, Department of Structural Engineering and Building Materials, Magnel-Vandepitte Laboratory, Technologiepark-Zwijnaarde 60, 9052 Ghent, Belgium
[b] Microlab, Section Materials and Environment, Faculty of Civil Engineering and Geosciences, Delft University of Technology, Stevinweg 1, 2628 CN Delft, the Netherlands
[c] Luchuan Ding, College of Civil Engineering, Tongji University, Shanghai 200092, China

ARTICLE INFO

Keywords:
Slag and fly ash-based alkali-activated concrete
Strength
Elastic modulus
Poisson's ratio
Prediction
Machine learning

ABSTRACT

In this paper, 871 data were collected from literature and trained by the 4 representative machine learning methods, in order to build a robust compressive strength predictive model for slag and fly ash based alkali activated concretes. The optimum models of each machine learning method were verified by 4 validation metrics and further compared with an empirical formula and experimental results. Besides, a literature study was carried out to investigate the connection between compressive strength and other mechanical characteristics. As a result, the gradient boosting regression trees model and several predictive formulas were eventually proposed for the prediction of the mechanical behavior including compressive strength, elastic modulus, splitting tensile strength, flexural strength, and Poisson's ratio of BFS/FA-AACs. The importance index of each parameter on the strength of BFS/FA-AACs was elaborated as well.

1. Introduction

During the past decades, promoting the utilization of blast furnace slag and fly ash based alkali activated concretes (BFS/FA-AACs) has gained increasing attention because it can alleviate carbon dioxide footprint and reduce waste disposal [1–3]. Nowadays, BFS/FA-AACs using sodium hydroxide and sodium silicate as alkali activated solution is the most widely investigated in the academic field. It maximizes the potential of all raw materials and creates concrete with the best overall performance [4–9].

Despite the advantages above, the compressive strength of BFS/FA-AACs approaches steady at 90 d with a probability of slightly changing later, compared with the 28 d strength development period for Portland cement concrete (PC concrete)[10]. Since it takes a long time for BFS/FA-AACs to achieve stable mechanical properties, the importance of strength prediction cannot be overemphasized. Accurate mechanical properties predicted methods of BFS/FA-AACs could effectively avoid waste of time, labor, and raw materials during the mix design process. However, there is no literature report on it by far. Therefore, an urgent task is to put forward robust mechanical properties prediction models for BFS/FA-AACs.

Studies have shown that the composition and concentration of alkali activators and components, as well as the quality of precursors, will affect the performance of slag and fly ash-based alkali-activated materials (BFS/FA-AAMs) [11,12]. Ouyang et al. [13] found that increasing sodium silicate modulus from 0 − 1.5 can improve the compressive strength of slag and fly ash based alkali activated paste (BFS/FA-AAPs). However, further increases from 1.5 − 2 could result in a decrease in strength due to the inhibition of the reaction process. Ramagiri et al. [14] reported that increasing BFS content from 0−50 % is associated with higher compressive strength of BFS/FA-AACs. Huseien et al. revealed that the splitting tensile strength and flexural strength of BFS/FA-AACs are better with higher BFS content due to the formation of more hydration products [15]. Although the results cannot be directly compared due to the inconsistent parameters in different literature and the combined effect of a large number of factors, the continuous publications make it possible to employ machine learning algorithms in compressive strength prediction.

Machine learning algorithms can build a predictive method based on a big data set without understanding the complex physical mechanism, which still has good accuracy and generalization ability, e.g. the artificial neural network, the support vector machine, the Gaussian regression method, the regression tree, the random tree, and the gradient boosting regression tree [16,17] Among all machine learning methods,

* Corresponding authors at: Ghent University, Department of Structural Engineering and Building Materials, Magnel-Vandepitte Laboratory, Technologiepark-Zwijnaarde 60, 9052 Ghent, Belgium.
E-mail addresses: g.ye@tudelft.nl (G. YE), Geert.DeSchutter@ugent.be (G. De SCHUTTER).

https://doi.org/10.1016/j.conbuildmat.2023.133933
Received 18 August 2023; Received in revised form 11 October 2023; Accepted 22 October 2023
Available online 27 October 2023

the random tree, the regression tree, the artificial neural network, and the gradient boosting regression tree are effective methods in evaluating the compressive strength of PC concrete [18–22]. The three tree-based regression methods are adopted to show the increasing improvement of the performance of the tree-based regression methods from single tree regression model to the random tree model, then to the more advanced gradient boosting regression tree. It can also be regarded as a quantitative comparison among the three tree-based methods, as well as a proof of that a more advanced method can result in a better result. On the other hand, the artificial neural network can be adopted as a representative of the other nonlinear regression models, because it usually shows almost the best performance in the other methods or it has a strong performance for nonlinear regression. Note that many kinds of machine learning methods with different degrees of accuracy class can be adopted to model the mapping relationship between the inputs and the outputs.

Given this, several machine learning studies have been done to establish the compressive strength predictive method of alkali-activated materials as well. For instance, Nazari et al. collected 399 data and developed a compressive strength predictive method for metakaolin-based alkali-activated concrete by artificial neural networks [23]. Nguyen et al. studied 355 data and proposed a compressive strength predictive method for fly ash-based alkali-activated materials based on a deep neural network and deep residual network [24]. Gomaa et al. built a compressive strength predictive method for fly ash-based alkali-activated materials by random forest and regression tree with 180 data [25]. Although there have been some attempts, the selected input parameters were either too numerous or too complicated to be used as mix design factors, and the databases were not sufficient to provide a robust predictive model. Regarding BFS/FA-AAMs, none of the existing studies investigated the compressive strength predictive method due to its unclear decisive factors.

The control factors have been extracted from the reaction mechanism point of view. It is revealed that these factors could also be the decisive parameters of BFS/FA-AAMs (including paste, mortar, and concrete) [26–28]. It provides a basis for machine learning and a guarantee of accuracy. Once a robust compressive strength prediction model of BFS/FA-AACs is built, the prediction models for the other mechanical properties (tensile strength, elastic modulus, etc.) of BFS/FA-AACs will be achieved with relationships. With this concept, in addition to building up the compressive strength prediction model of BFS/FA-AACs, it is meaningful to clarify the connections between compressive strength and other mechanical behaviors of BFS/FA-AACs.

In this paper, four representative machine learning methods are used to fit the 871 data collected from the existing literature and build predictive models. By validation and comparison, a robust compressive strength predictive model for BFS/FA-AAMs has been developed. The connections between compressive strength and other mechanical characteristics (Poisson's ratio, splitting tensile strength, elastic modulus, and flexural strength) have been quantitatively clarified, and the predictive formulas for the other mechanical behaviors of BFS/FA-AACs were proposed. Moreover, the importance index of each model parameter on the compressive strength of the BFS/FA-AAMs is derived, which contributes to the mix design approaches of BFS/FA-AAMs.

2. Machine learning procedure

2.1. Collection of the BFS/FA-AAM database

A large database with significant variations in both input (control factors) and output (compressive strength) was built from the literature. In total, 871 data (871 mix proportions of BFS/FA-AAMs and their corresponding compressive strength) were collected [10,14,15,30–51]. Literature characterizing geopolymers and alkali-activated materials were studied. Concrete, paste, and mortar are all included in the data. The chosen mix proportion ranges in compressive strength from 0.34 to 117.26 MPa, in Na_2O/b ratio from 1.3 % to 14.41 %, in SiO_2/Na_2O ratio from 0 to 2.63, in w/b ratio from 0.22 to 0.73, in curing time from 1 to 180 days, and in ambient curing temperature. The 5 input parameters have been proven of the control factors of the compressive strength of BFS/FA-AAM [26–28]. It is worth noting that the compressive strength of BFS/FA-AAM is predominated by the strength of paste as it is the weakest region. The interfacial transition zone BFS/FA-AAM is reported to be denser, more cohesive, and uniform because the bonding of aggregate and paste is improved by the soluble Si and expansive Al-free gels are less generated [52–58].

The objective is to learn and analyze the data with 4 machine learning models, to examine all the possible effective machine methods reported in the literature, and to filter out the most accurate method. Specifically, the compressive strength of BFS/FA-AAMs was set as the target (output *Y*), which is a function of the following five input parameters: Na_2O/b (input *X1*), SiO_2/Na_2O (input *X2*), w/b (input *X3*), BFS/b (input *X4*), and curing time (input *X5*). Among these parameters, the Na_2O/b ratio refers to the mass of the Na_2O component to the mass of the BFS and FA ratio; the SiO_2/Na_2O ratio refers to the mass of the SiO_2 component to the mass of the Na_2O component ratio; the w/b ratio refers to the mass of water to the mass of BFS and FA ratio; the BFS/b ratio refers to the mass of BFS to the mass of BFS and FA ratio.

According to previous research, the input parameters of BFS/FA-AAMs (curing in ambient temperature) are the most representative factors of compressive strength [26,27]. Although different studies reported different mix design parameters (eg: NaOH/Na_2SiO_3 ratio, l/b ratio, w/Na_2O, Na_2SiO_3/b ratio, curing time, etc.) and different chemical compositions of raw materials (eg: the molar ratio of Na_2SiO_3 and NaOH concentration,), all the mix proportions were eventually transferred to the 5 control factors by calculation. The variable statistical information and the distributions are presented in Table 1 and Fig. 1, respectively.

2.2. Gradient boosting regression tree

The gradient boosting decision tree, as an individual learning algorithm, is one of the widely used boosting approaches [59–62]. The concept behind boosting ensemble learning is to integrate several ineffective weak learners into one powerful strong learner for prediction. At each step, a subsequent model (weak learner) related to an individual learning algorithm is created to boost training cases that are not well predicted by the previous weak learner. Through the continuous revision of the model, a strong learner could be eventually formed by the aggregation of the weak learners. In this research, the decision tree algorithm was adopted as the weak learners, The gradient boosting regression trees model (GBRT) was utilized for regression, and the negative gradient of the loss function was applied. The procedure concerning the GBRT model is illustrated in Fig. 2.

Generally, GBRT could predict the output value (compressive strength) for a given input (control factors) by Eq. (1).

$$Y \approx \widehat{Y} = F_M(X) = \sum_{m=1}^{M} h_m(X,\ \theta_m) \tag{1}$$

In which: Y is the target output value, X is the given input, h_m is an estimator (or a weak learner), $\hat{I}_{,}$ is the fixed size of the regression tree, M is the total number of weak learners.

A classic GBRT in the academic field is a regularization technique that scales each weak learner's contribution, as shown in Eq. (2) [63]. This formula adds a learning rate to adjust the gradient descent procedure's step size. Generally, The total number of weak learners needed to maintain a steady training error and a low test error increases with decreasing learning rate and decreases test error [61]. It has been recommended to choose the total number of weak learners by early halting and to set the learning rate lower than 0.1 [63].

Table 1
Statistical information of the collected data.

Variable	Name	Unit	Min.	Max.
Input *X1*	Na_2O/b	%	1.30 [38]	14.41 [30]
Input *X2*	SiO_2/Na_2O	–	0.00 [45]	2.63 [46]
Input *X3*	w/b	–	0.22 [32]	0.73 [48]
Input *X4*	BFS/b	–	0.00 [10,14,29,32,34,35,38]	1.00 [10,36,37,39,43–46,48]
Input *X5*	Curing time	days	1.00 [10,29,31]	180.00 [32,50]
Output *Y*	Compressive strength	MPa	0.34 [34]	117.26 [10]

Note: the Na_2O/b ratio refers to the mass of the Na_2O component to the mass of the BFS and FA ratio; the SiO_2/Na_2O ratio refers to the mass of the SiO_2 component to the mass of the Na_2O component ratio; the w/b ratio refers to the mass of water to the mass of BFS and FA ratio; the BFS/b ratio refers to the mass of BFS to the mass of BFS and FA ratio.

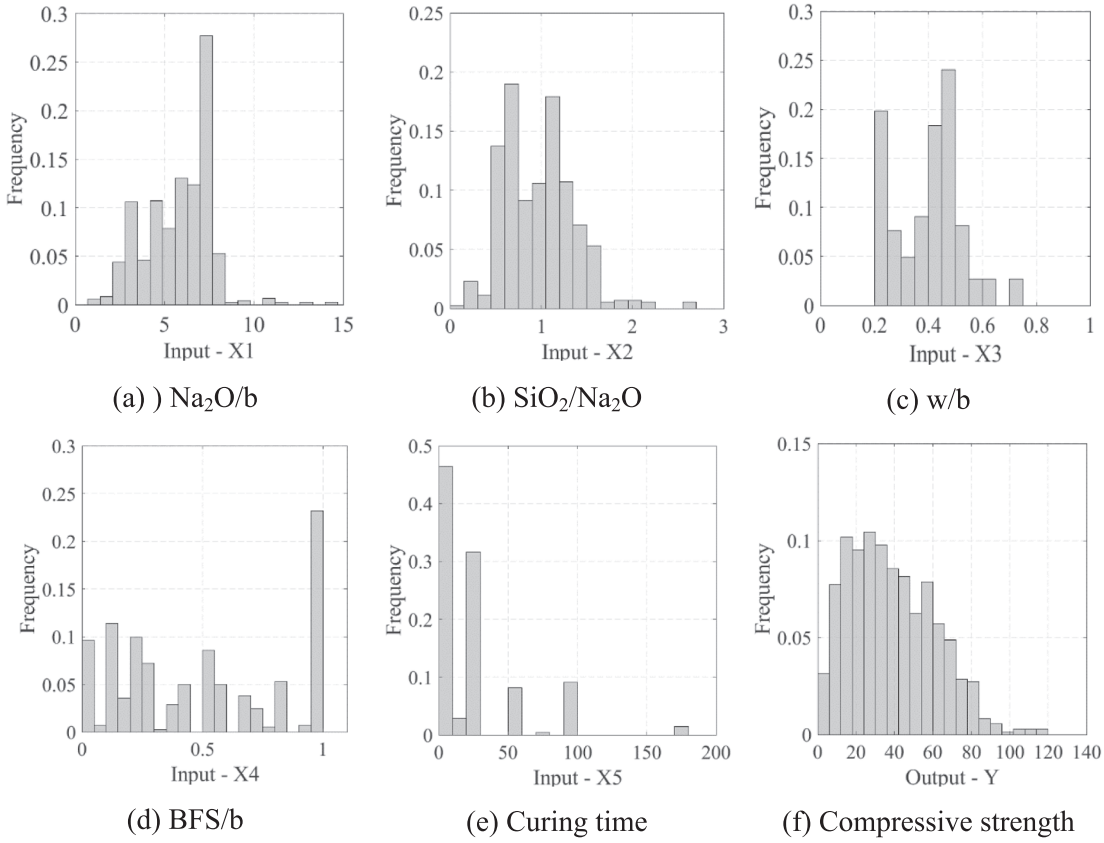

Fig. 1. Statistical distributions of both input and output variables.

$$F_m(X) = F_{m-1}(X) + \hat{I}½h_m(X,\ \hat{I}_{,m}) = \hat{Y} \tag{2}$$

In which: ν is the learning rate;

In this research, a newly add weak learner h_m is fitted at each iteration until the regression times reach the total. To minimize a sum of losses regarding the prior ensemble prediction value, h_m is fitted according to Eq. (3) [62]. By default, the initial predictive value (F_0) is chosen as a constant that minimizes the loss. For a least-squares loss, it is given by the mean of the compressive strength of BFS/FA-AAMs.

$$h_m = Y\text{-}F_{m-1}(X) = \underset{h_m}{\operatorname{argmin}} L_m = \underset{h_m}{\operatorname{argmin}} \sum_{i=1}^{n} l(y_i,\ F_{m-1}(x_i) + \hat{I}½h_m(x_i,\ \hat{I}_{,m})) \tag{3}$$

In which: L_m is the sum of the loss, $l(y_i, F(x_i))$ is the least-squares loss.

By using a first-order Taylor approximation at $F_{m-1}(x_i)$, the least-squares loss can be approximately calculated (see Eq. (4)).

$$l(y_i, F_{m-1}(x_i) + h_m(x_i, \theta_m)) \approx l(y_i, F_{m-1}(x_i)) + \nu h_m(x_i,\ \theta_m)[\partial l(y_i, F(x_i))/\partial F(x_i)]_{F=F_{m-1}} \tag{4}$$

Considering Eq. (3) and Eq. (4), the h_m could be eventually calculated with Eq. (5)

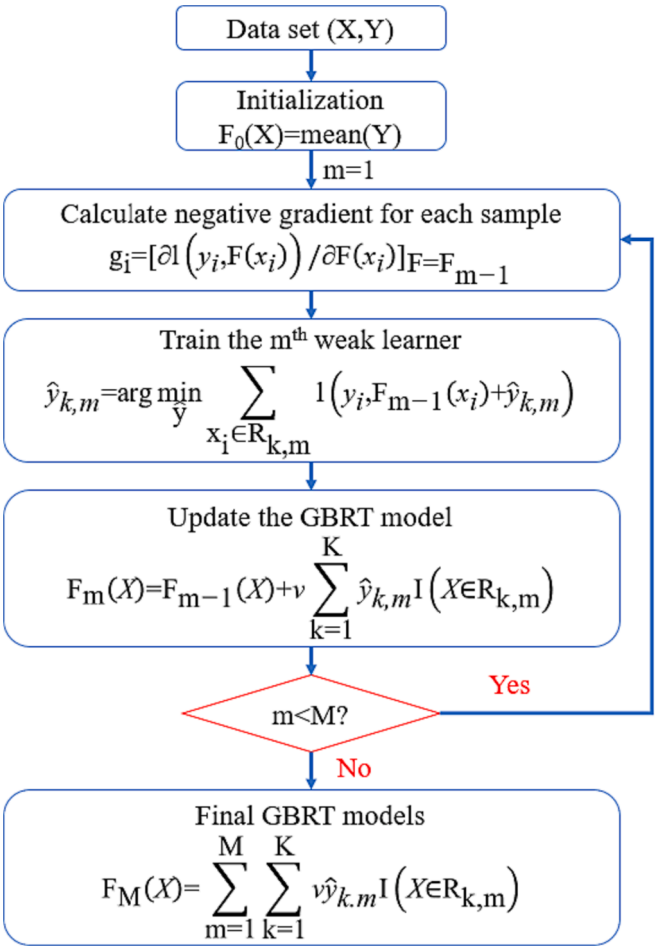

Fig. 2. Illustration of the GBRT model.

$$h_m \approx \underset{h_m}{\operatorname{argmin}} \sum_{i=1}^{n} \{ l(y_i, F_{m-1}(x_i)) + \nu h_m(x_i, \theta_m) g_i \} \tag{5}$$

The quantity $g_i = [\partial l(y_i, F(x_i))/\partial F(x_i)]_{F=F_{m-1}}$ is the derivative of the loss concerning its second parameter at $F_{m-1}(X)$. For any given $F_{m-1}(X)$ in a closed form, it could be calculated since the loss is differentiable. When the constant terms are removed in Eq. (5), a simplified calculation of h_m could be obtained (see Eq. (6)).

$$h_m \approx \underset{h_m}{\operatorname{argmin}} \sum_{i=1}^{n} \nu h_m(x_i, \theta_m) g_i \tag{6}$$

The weak learner h_m is fitted to anticipate the negative gradients of the samples at each iteration. If $h_m(x_i, \hat{I}_{,m})$ at each iteration is fitted to predict a value that proportionates to the negative gradient $-g_i$, the weak learner could be minimized. Each iteration involves updating the gradients, which is known as gradient descent in a function space. A regression tree can partition the X region into disjoint regions $R_{k,m}$ (k = 1, 2, …, K) at each iteration *m*. This is presuming the weak learner $h_m(x_i, \hat{I}_{,m})$ is a *K* terminal node regression tree. A separate constant value could be predicted for each region based on a least-squares splitting criterion and a top-down, best-fit method [58]. Therefore, $h_m(x_i, \hat{I}_{,m})$ could be calculated by Eq. (7).

$$h_m(x_i, \theta_m) = \sum_{k=1}^{K} \hat{y}_{k,m} I(X \in R_{k,m}) \tag{7}$$

In which: $\hat{y}_{k,m}$ is the mean fitted values of each region $R_{k,m}$, I is the indicator function.

For the k^{th} leaf region, the optimized value for $\hat{y}_{k,m}$ could be calculated by Eq. (8).

$$\hat{y}_{k,m} = \underset{\hat{y}}{\operatorname{argmin}} \sum_{x_i \in R_{k,m}} l(y_i, F_{m-1}(x_i) + \hat{y}_{k,m}) \tag{8}$$

Accordingly, an updated stronger learner at the m^{th} iteration could be expressed by Eq. (9).

$$F_m(X) = F_{m-1}(X) + \nu h_m(X, \theta_m) = F_{m-1}(X) + \nu \sum_{k=1}^{K} \hat{y}_{k,m} I(X \in R_{k,m}) \tag{9}$$

After M iteration, the GBRT model can be obtained, as shown in Eq. (10).

$$\hat{Y} = F_M(X) = \sum_{m=1}^{M} \sum_{k=1}^{K} \nu \hat{y}_{k,m} I(X \in R_{k,m}) \tag{10}$$

Based on the above algorithm, a Python module called Scikit-learn [64] was used in this research to create the GBRT model. It integrates various methods for medium-scale applications [64]. The implementation of the GBRT model can be summed up as follows:

1) To divide the collected database into a training set (80 % of the data) for developing the model, and a testing set (the rest 20 % of the data) for evaluating the model [59,60,65].
2) To train the weak learners (regression trees) with the training set. To assess the effectiveness of the trained model with the testing set. Eventually, to obtain the GBRT model with an ensemble of amounts of weak learners.
3) To apply the GBRT model into practice.

The hyper-parameters for the GBRT model, which may significantly affect its performance, cannot be directly learned in the training process. These hyper-parameters include the number of weak learners, the learning rate, the maximum depth of the tree, the maximum number of leaf nodes, the minimum number of samples needed to be at a leaf node, and the minimum number of samples needed for splitting an internal node. Nonetheless, they could be tuned through the application of the grid search method. Specifically, the ranges of these hyper-parameters

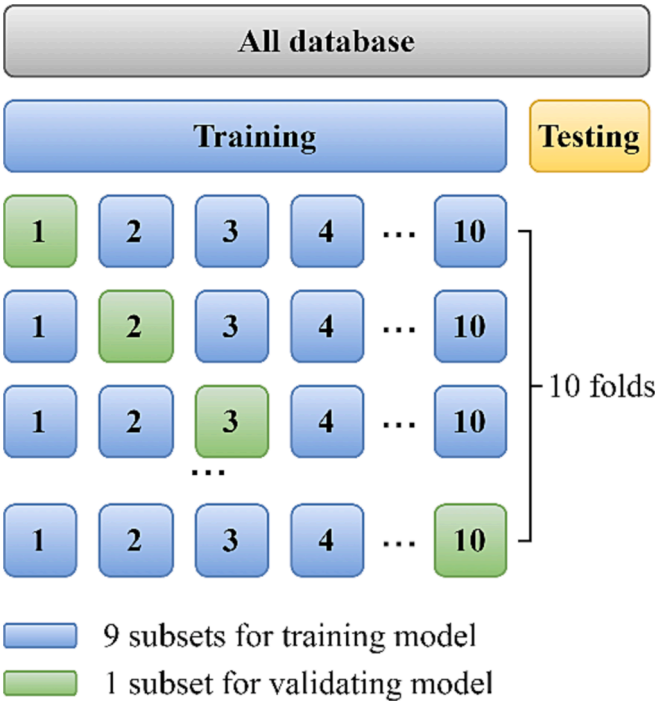

Fig. 3. 10-fold cross-validation.

could be predefined and the optimal parameter in the grid of the ranges could be further selected with a 10-fold cross-validation approach, which is known for evaluating the model effectiveness (see Fig. 3). In this research, the following ranges were predefined for the hyper-parameters concerning the GBRT model: the number of weak learners [2:2:500], the learning rate [0.01, 0.05, 0.1, 0.2, 0.3, 0.4, 0.5], the maximum depth of the tree [1:1:10], the maximum number of leaf nodes [2:1:20], the minimum number of samples required to be at a leaf node [1:1:20], and the minimum number of samples needed for splitting an internal node [2:1:20]. The training set was further divided evenly into 10 subsets, in which 9 subsets were utilized to train the model, and the last subset was used for validation. As each lop, 10 GBRT models were obtained, and the average of the validation values was calculated and reported as an output. By comparison, the optimal hyper-parameters were selected and further combined to build the best GBRT model.

2.3. Random forests

An ensemble method called random forests (RF) fits numerous decision trees and addresses both classification and regression issues on diverse sub-samples of the dataset. To increase the forecast accuracy and prevent over-fitting, the individual tree's averaged prediction is employed. Previous researchers have shown that RF is an effective machine learning technique for prediction without over-fitting based on the law of large numbers [60,66–68]. Compared with the boosting technique of GBRT, the bagging technique is adopted in RF [68].

To develop an RF model for predicting the compressive strength of BFS/FA-AAMs, 80 % of the data (training set) was utilized to train the RF model, while the rest 20 % of the data (testing set) was adopted for validation. Scikit-learn [64] was used to develop and tune the RF model. To tune the hyper-parameters in the training stage, the grid search method combined with 10-fold cross-validation was adopted. In total five hyper-parameters were tuned including the number of regression trees, the maximum depth of the tree, the maximum number of leaf nodes, the minimum number of samples required to be at a leaf node, and the minimum number of samples needed for splitting an internal node. The predefined grids for these five parameters were set as [2:2:200], [1:1:10], [2:1:20], [1:1:20] and [2:1:20], respectively.

2.4. Regression tree

A non-parametric supervised learning technique known as an individual regress tree (RT) is conceived of as a piecewise constant approximation [67,69,70]. In this research, 80 % of the data (training set) was adopted for training the RT model, while the rest 20 % of the data was used as the testing set. Scikit-learn [64] was used to create an RT model. The grid search method was used in conjunction with 10-fold cross-validation to fine-tune the hyper-parameters in the training stage. Four parameters were tuned, which include: the maximum depth of the tree, the maximum number of leaf nodes, the minimum number of samples required to be at a leaf node, and the minimum number of samples needed for splitting an internal node. The predefined grids for the four parameters were set as [1:1:10], [2:1:20], [1:1:20] and [2:1:20], respectively.

2.5. Artificial neural network

Artificial neural network (ANN) is an approach for tackling complex problems through the use of nonlinear data-driven models [60,71–73]. The ANN toolbox in MATLAB (nftool) was adopted in this research [73,74]. To resolve multi-dimensional mapping issues, a feed-forward network with two layers which has sigmoid hidden neurons and linear output neurons was fitted. The Levenberg-Marquardt backpropagation algorithm was adopted to adjust the connection weights and bias values during training. 80 % of the data were applied for training (training set), 10 % were employed for validation (validating set), and the rest 10 % were utilized for testing (testing set).

2.6. Model validation

To determine the predictive effectiveness of the models, the four widely used metrics were adopted to quantify their performance, including coefficient of determination (R^2), root mean squared error (RMSE), mean absolute percentage error (MAPE), mean absolute error (MAE), as presented in Eqs. (11)–(14) [60,68].

$$R^2 = 1 - \sum_{i=1}^{N} \left(y_{Predicted,\,i} - y_{Tested,\,i}\right)^2 / \sum_{i=1}^{N} \left(y_{Tested,\,i} - \overline{y_{Tested}}\right)^2 \tag{11}$$

$$RMSE = \sqrt{\sum_{i=1}^{N} \left(y_{Predicted,\,i} - y_{Test,\,i}\right)^2 / N} \tag{12}$$

$$MAPE = \frac{100\%}{N} \sum_{i=1}^{N} \left| y_{Predicted,\,i} - y_{Tested,\,i} \right| / y_{Tested,\,i} \tag{13}$$

$$MAE = \sum_{i=1}^{N} \left| y_{Predicted,\,i} - y_{Tested,\,i} \right| / N \tag{14}$$

In which: $y_{Predicted,\,i}$ is the predictive value, $y_{Tested,\,i}$ is the experimental value, $\overline{y_{Tested}}$ is the average value of the experimental value, and N is the total number of samples.

The coefficient of determination (R^2) is a measurement of how well the regression line approaches the actual data. A higher value between 0 and 1 is associated with the stronger explanatory power of the regression model. The discrepancy between the predictive value and the experimental value is represented by the sample standard deviation as the root mean square error (RMSE). The disparity between them increases as the RMSE value increases. Due to its intuitive interpretation with regard to relative error, mean absolute percentage error (MAPE) is frequently employed as a loss function for regression issues. The error between two observations reflecting the same occurrence is measured by mean absolute error (MAE). A high-precision model is normally associated with low MAPE and MAE values.

3. Results and discussions

3.1. Compressive strength prediction

3.1.1. Machine learning models

3.1.1.1. Compressive strength prediction by the GBRT model. Regarding the GBRT model, the following optimized hyperparameters were determined by the grid search method: the number of weak learners is 500, the learning rate is 0.1, the maximum depth of the tree is 4, the maximum number of leaf nodes is 6, the minimum number of samples required to be at a leaf node is 11, and the minimum number of samples needed for splitting an internal node is 9. It is known that a GBRT model can reach better performance if more weak learners are incorporated. As indicated in Fig. 4(a), the RMSE values during the training stage (loss function) decrease with the addition of more weak learners (individual regression tree), which represents a better prediction. However, the increase in performance is negligible after the number of weak learners reaches 400. Therefore, the final optimized hyper-parameter for the number of weak learners was selected as 400. The R^2, RMSE, MAPE, and MAE of the testing set are 0.94, 5.58, 14.2, and 3.97, respectively. The values for R^2 are approaching unity and the values for RMSE, MAPE, and MAE are small, reflecting a satisfied performance of the GBRT model. A highly linear positive correlation could be observed between predictive strength and actual strength in both the training set and the testing set, which further illustrates the robustness of the GBRT model (see Fig. 4(b, c)). It also demonstrated how the model parameters primarily affect the

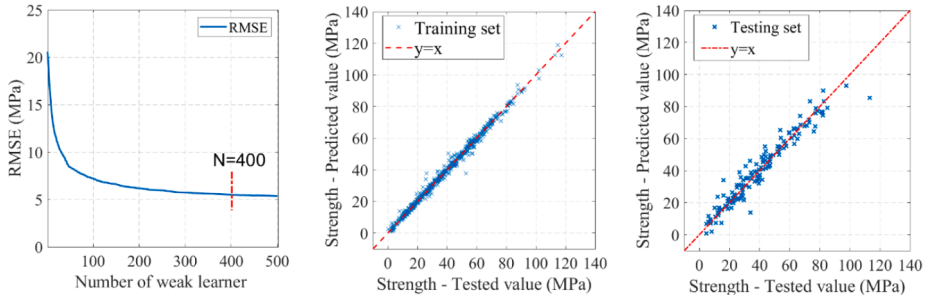

(a) Parameter tuning (b) Comparison of the training set (c) Comparison of the testing set

Fig. 4. Results of GBRT.

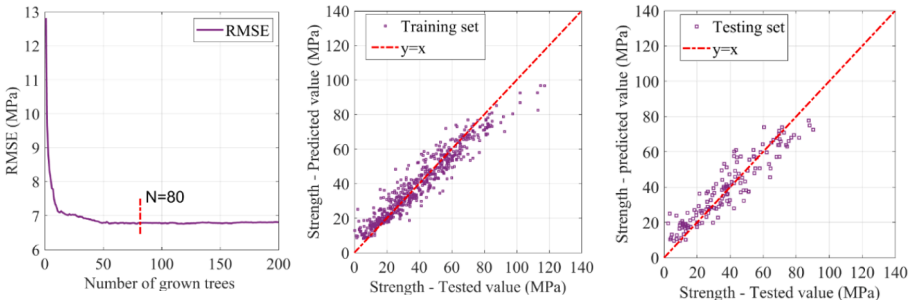

(a) Parameter tuning (b) Comparison of the training set (c) Comparison of the testing set

Fig. 5. Results of RF.

compressive strength of BFS/FA-AAMs.

3.1.1.2. Compressive strength prediction by the RF model. Regarding the RF model, the hyper-parameters: the number of regression trees, the maximum depth of the tree, the maximum number of leaf nodes, the minimum number of samples required to be at a leaf node, and the minimum number of samples needed for splitting an internal node were tuned and selected to be 200, 5, 17, 2, and 2, respectively. As shown in Fig. 5(a), when the number of trees surpasses 80, the performance of the RF model is only slightly improved. Consequently, the optimal value for the number of trees is 80. The values of R^2, RMSE, MAPE, and MAE values of the testing set are 0.85, 8.10, 34.0, and 6.43, respectively. The predicted compressive strength values and the experimental compressive strength values exhibit a strong linear positive correlation in both training and testing sets (see Fig. 5(b, c)).

3.1.1.3. Compressive strength prediction by the RT model. According to the tuning results of the RT model, the optimized hyper-parameters: the maximum depth of the tree, the maximum number of leaf nodes, the minimum number of samples required to be at a leaf node, and the minimum number of samples needed for splitting an internal node are 6, 19, 1, and 2, respectively. The values of R^2, RMSE, MAPE, and MAE for the testing set are 0.73, 11.00, 36.4, and 8.57, respectively. Similarly, there is a positive linear correlation between predictive strength and experimental strength (see Fig. 6).

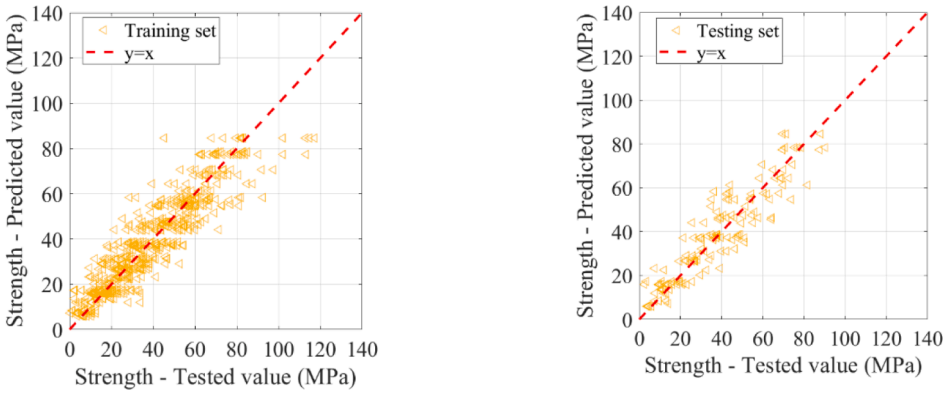

Comparison of the training set Comparison of the testing set

Fig. 6. Results of RT.

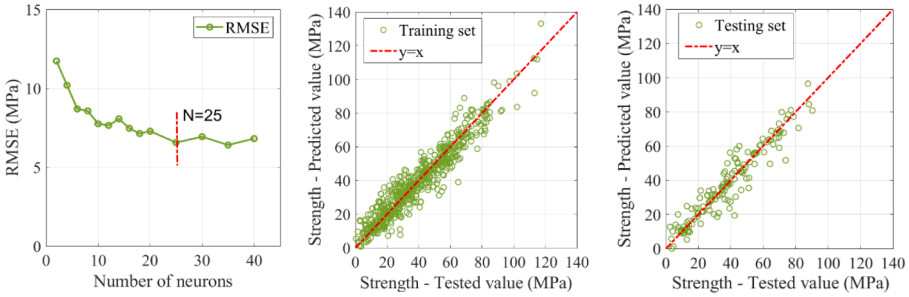

(a) parameter tuning (b) Comparison of the training set (c) comparison of the testing set

Fig. 7. Results of ANN.

3.1.1.4. Compressive strength prediction by the ANN model. The only parameter required to be set for the ANN model is the number of neurons in the hidden layer. To optimize this parameter, ANN models with different numbers of neurons in the hidden layer were trained and the corresponding root means squared errors on the testing set are presented in Fig. 7. (a). It shows that the RMSE first decreases with the increasing number of neurons in the hidden layer and then stabilizes after the number of neurons surpasses 25. Therefore, the optimized hyperparameter for the ANN model is 25. The comparison between the corresponding predicted values using the ANN model and the experimental values on both the training set and the testing set are presented in Fig. 7 (b, c). The values of R^2, RMSE, MAPE, and MAE on the testing set are 0.90, 6.56, 20.7, and 4.61, respectively.

3.1.1.5. Comparison of compressive strength prediction by the four models. For comparison, 4 performance metrics were used for evaluating the efficiency of the above machine learning models. As displayed in Table 2, the results indicate that the GBRT model has the highest accuracy among all predictive models. A second-best performance is observed for the ANN model. Among the three tree-based methods, the tree-based methods (GBRT and RF) have a better performance than the individual tree-based method (RT).

From the above validation, it can be seen that the accuracy of the above machine learning models is high, indicating the compressive strength of BFS/FA-AAMs is significantly influenced by the model parameters. Each parameter varies in its contribution to the compressive strength of BFS/FA-AAMs, depending on the corresponding effect mechanism [26,27].

3.1.2. Importance of parameters

3.1.2.1. Model inspection technique. In this research, a model inspection technique was used to further assess how much influence each parameter has on the compressive strength of BFS/FA-AAMs. By breaking the relationship between the output variable and each input variable (randomly shuffling the input variable) [64], and successively applying the best-trained GBRT model, 5 descended R^2 scores could be obtained. The difference between them and the reference score is considered the importance score of each input variable, which represents how dependent the model is on the input variable. The implemented algorithm is listed as follows:

1) The reference score S (R^2) of the fitted GBRT model on the training set D=(X, Y) was first computed: $S = 0.99$;
2) For each input variable j (j = 1,2,…, the total number of model parameters) from the training set D, and for each repetition r (r = 1,2, …, total repeat times), a corrupted version of the data $D_{r,j}$ was prepared by randomly shuffle column j. Afterwards, the reference score $S_{r,j}$ of the GBRT model on corrupted data $D_{r,j}$ was calculated.
3) The importance score S_j for the input variable j was calculated as Eq. (15):

$$S_j = S - \frac{1}{c}\sum_{r=1}^{R} S_{r,j} \tag{15}$$

According to the model inspection results, the importance scores for the model parameters of BFS/FA-AAMs are illustrated in Fig. 8(a). The comparisons between the predictive values and the experimental values of the training set are demonstrated in Fig. 8(b–f) concerning different model parameters (*X1-X5*). The more discrete the data, the more significant the factor can affect the compressive strength.

With the highest importance score of 1.20, it shows that the BFS/b ratio (*X4*) is a key parameter of the compressive strength of BFS/FA-AAMs. The curing time (*X5*) is the second most important parameter of the compressive strength, with an importance score of 0.75. The importance score for the Na_2O/b ratio (*X1*) and SiO_2/Na_2O ratio (*X2*) is 0.32 and 0.24, respectively. The importance score for the w/b ratio (*X3*) is the lowest, indicating that the formation of compressive strength is least affected by water, which is the opposite of cement-based materials.

The above observation is consistent with the previous research [26,27]. Regarding compressive strength, the dominant effect of the BFS/b ratio is associated with the composition of chemicals in precursors. A higher content of BFS in the reaction systems can lead to a faster dissolution rate due to introducing a higher amount of Ca. Therefore, BFS/FA-AAMs exhibit higher compressive strength as the BFS/b ratio rises. The effect of curing time is of great importance since it is decisive for microstructure development. Despite that BFS/FA-AAMs featuring a low BFS/b ratio typically requires a longer curing time, the 90 days of curing time is revealed to be sufficient for the compressive strength of BFS/FA-AAMs to achieve stability. The growth of the Na_2O/b ratio will enhance the mechanical behavior of BFS/FA-AAMs because of the formation of an intenser alkali condition which stimulates the dissolution of precursors. Nonetheless, excessive Na_2O content can hinder further dissolution in a short period with the generation of a calcium hydroxide layer on the surface of precursors, which causes the reduction of the compressive strength. The increase in the SiO_2/Na_2O ratio benefits the strength of BFS/FA-AAMs because the soluble Si can absorb the dissolved reaction ions. Microstructure with less porosity can be produced with higher content of NCASH gels occupying the solution. However, the mechanical properties can be hindered as the SiO_2/Na_2O

Table 2
Performance metrics.

Performance metrics	R^2 (-)	RMSE (MPa)	MAPE (%)	MAE (kN)
GBRT	0.94	5.58	14.2	3.97
RF	0.85	8.10	34.0	6.43
RT	0.73	11.00	36.4	8.57
ANN	0.90	6.56	20.7	4.61

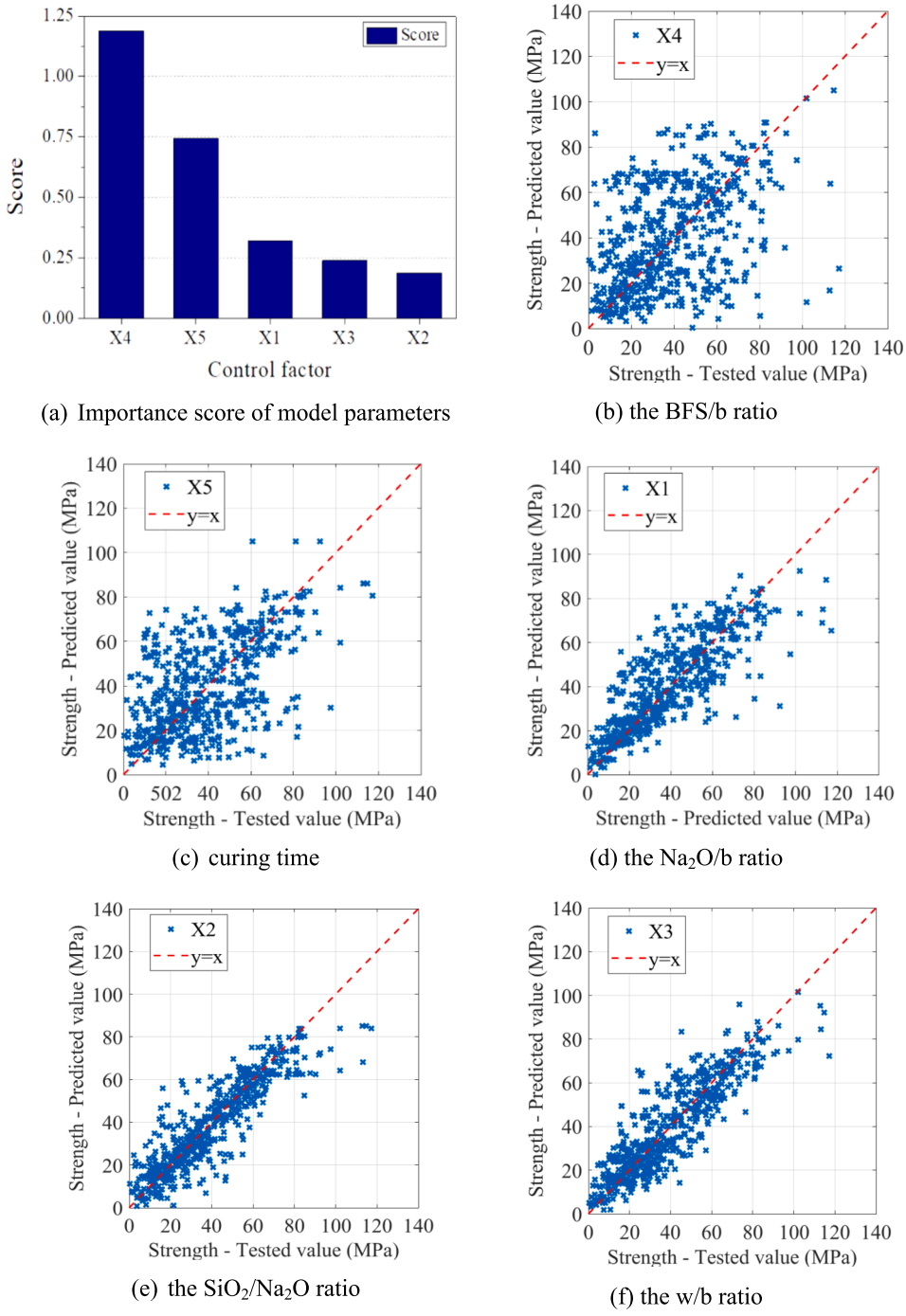

Fig. 8. The importance scores and ranking of model parameters.

ratio exceeds a particular value. This is caused by the surface of the precursor particle being covered by Si layer. Water content has a less substantial influence on compressive strength than other parameters since water merely performs as a carrier of alkali elements during the polymerization process.

3.1.3. Validation

For BFS/FA-AAPs, previous research has proposed a predictive formula (PF) for predicting compressive strength, as listed in Eq. (16) [27]. This formula is the result of a methodical examination of the parameters that affect the compressive strength of it. Polynomial surface fitting and curve fitting based on least-squares were combined to derive the predictive formula. Its efficiency has also been validated on BFS/FA-AACs by experiments because the interfacial zone is no longer the weakest link in alkali-activated materials [28].

$$Y = \left(-1.33 + 12.3X_1 + 42.68X_2 - 1.04X_1^2 + 2.37X_1X_2 - 17.05X_2^2\right)$$

$$\cdot(-1.37X_3 + 1.04X_4 + 1)\cdot 0.2\ln(X_5 + 11.31) \quad (16)$$

To verify the validity of Eq. (15) on BFS/FA-AAMs with a larger database, the collected data were used as the testing set. According to the results, the values of R^2, RMSE, MAPE, and MAE on the testing set are 0.56, 14.58, 78.16, and 12.13, respectively. The relatively low predictive accuracy is because a large part of the samples was cured at the unsealed condition, which lead to remarkably fluctuating compressive strength. Besides, some of the mixture proportions in the testing set

surpass the application limitation of Eq. (16). It is worth pointing to the condition of Eq. (16): the BFS/b ratio between 0 and 1, the SiO_2/Na_2O ratio between 0 and 2, the Na_2O/b ratio between 2 % and 10 %, the w/b ratio between 0.3 and 0.5, sealed and cured at room temperature. Sealed curing has been proven of promising for preventing possible efflorescence [27]. The data selected in this research includes both sealed and unsealed specimens because the current database on sealed curing is limited. It is suggested to further study the compressive strength model with sealed specimens when there is sufficient research.

The limitation is eliminated by the GBRT model. With the machine learning method, a larger database with a wider range can be added to re-evaluate the aforementioned empirical predictive formula. The best machine learning model (GBRT) and the empirical predictive formula (PF) were tested for accuracy and further validated by the experimental results of a previous study [28]. The comparison between the test value, formula predicted value, and model-predicted value of BFS/FA-AACs for various parameter combinations are shown in Fig. 9. All the samples are within the using condition of both predictive models. Moreover, a Wilcoxon signed-rank test was conducted using statistical product and service solutions (SPSS) for statistically assessing the effectiveness of the two models. Wilcoxon signed-rank test is suitable for pairwise comparison, while a symmetric distribution is needed, not a normal distribution, for the difference of paired data. It determines whether a population processing an average of 0 is responsible for the discrepancy between paired observations.

As demonstrated in Fig. 9(b–d) and Table 3, for prediction of over 7 d, good performance is observed for both the PF and the GBRT model. The P values (a parameter used to assess the significant difference of the compared samples) of both models were higher than 0.05 suggesting the differences are statistically insignificant. However, The median of the difference (the test value was subtracted from the predicted value) of the PF model is 4 times higher than that of the GBRT model.

The PF and the GBRT model show different performances in the 1 d prediction, as presented in Fig. 9(a) and Table 3. Both of them have some noticeable differences from the test value, though the predictive result by the GBRT model could be preferable in general. According to the results, the median difference between the test value and the PF model predicted value is about 3 times larger than that of the test value and the GBRT predicted value. The P-value of both models is 0, indicating statistically significant differences among them. It is consistent with previous research, which reports that the BFS/FA-AAPs mixture could need longer than three days for the compressive strength to begin growing [27].

Table 3
Wilcoxon signed-rank test results.

Predictive model	Median value (MPa)	Median of the difference with test value (Mpa)	P-value
PF (1d)	27	13.02	0
GBRT (1d)	17	4.37	0
PF (>7d)	38	−0.78	0.77
GBRT (>7d)	40	0.17	0.82

Although the methods and concepts of PF and GBRT models are different, both of them are capable of determining the compressive strength of BFS/FA-AACs with a curing time of longer than 7 d. The PF model predicts the compressive strength by understanding how and to what extent the parameters affect it, while the applying scale is relatively smaller than the GBRT model. Specifically, the applying scale of the GBRT model is: the Na_2O/b ratio between 1.3 % and 14.4 %, the SiO_2/Na_2O ratio between 0 and 2.6, the w/b ratio between 0.22 and 0.73, the BFS/b ratio between 0 and 1, and cured at room temperature. The GBRT model is predictive of the compressive strength by learning from big data and numerical approximation, while the adjusting method of mixture composition according to the compressive strength is agnostic. By comparison, the GBRT model exhibits greater accuracy than the PF model.

3.2. Other mechanical properties prediction

Besides the compressive strength, the other mechanical behaviors of of BFS/FA-AACs, such as: splitting tensile strength, flexural strength,

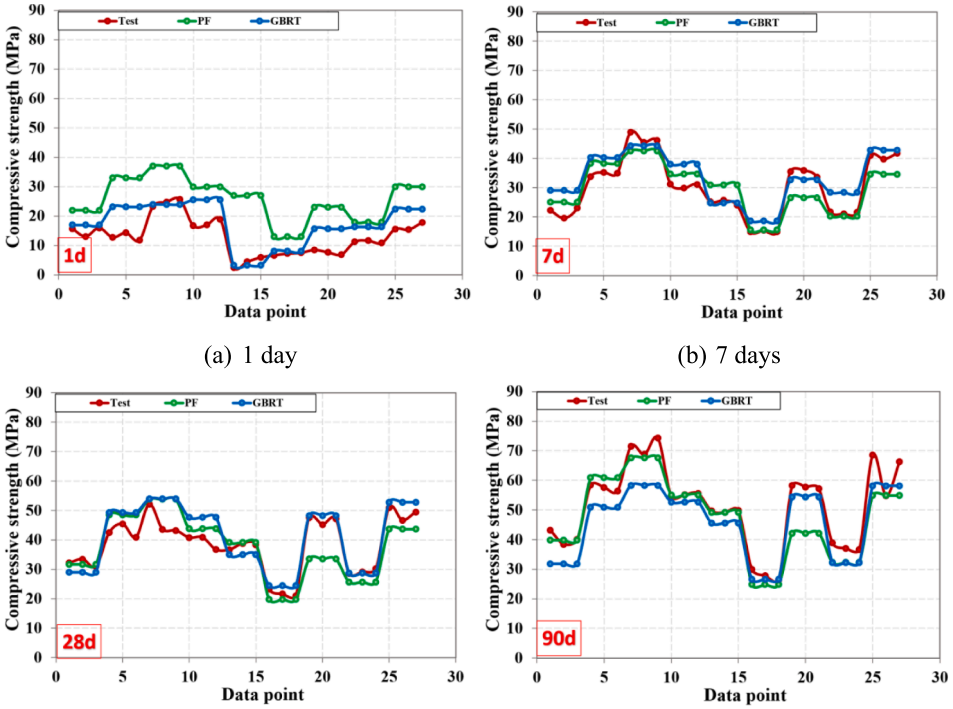

(a) 1 day (b) 7 days

(c) 28 days (d) 90 days

Fig. 9. Comparison between test value, PF predicted value and GBRT predicted value.

elastic modulus, and Poisson's ratio also play crucial parts in the engineering application. The accurate determination of compressive strength facilitates the estimation of the other mechanical properties since there is a close relationship between them. Due to the database difference, it is worth striking that the GBRT model is applicable for concrete, paste, and mortar, while the proposed predictive formulas in section 3.2 are applicable for concrete.

3.2.1. Splitting tensile strength

Through collecting correlated data from the existing literature and fitting, the connection between splitting tensile strength and compressive strength of BFS/FA-AACs is presented in Fig. 10 [7,33,42,44,75–86]. It is revealed that splitting tensile strength increase with the higher compressive strength of BFS/FA-AACs. The functional relationships between compressive strength (f_c') and the splitting tensile strength (f_{sp}) of BFS/FA-AACs are similar to the relationships of PC concrete in both American Concrete Institute standard (ACI standard) [87] (see Eq. (18)) and European standard (Eurocode) [88] (see Eq. (19)–(20)), though the parameters could be slightly different. Specifically, the splitting tensile strength of BFS/FA-AACs can be predicted by Eq. (17). The fitted curve of BFS/FA-AACs and the curve of PC concrete from the American standard have the highest similarity, which is almost identical. While the splitting tensile strength of BFS/FA-AACs can be slightly overestimated by the European standard of PC concrete. The standard error is 0.01 and the R^2 value is 0.61.

$$f_{sp} = 0.58\sqrt{f_c'} \tag{17}$$

$$f_{sp} = 0.56\sqrt{f_c'} \tag{18}$$

$$f_{sp} = 0.33 f_c'^{\frac{2}{3}}, f_c' \leqslant 50\ MPa \tag{19}$$

$$f_{sp} = 2.36\ln[1 + (f_c' + 8)/10], f_c' > 50\ \text{MPa} \tag{20}$$

In which: f_{sp} is the splitting tensile strength of BFS/FA-AACs (MPa),f_c' is the compressive strength of BFS/FA-AACs (MPa).

3.2.2. Flexural strength

The connection between flexural strength and compressive strength collected from the existing literature on BFS/FA-AACs is shown in Fig. 11 [44,75,77–79,89–91]. It is observed that higher flexural strength (f_r) is associated with higher compressive strength. This is consistent with that of PC concrete, according to the ACI standard (see Eq. (22)) and Eurocode (see Eq. (23)–(24)). The fitted curve of BFS/FA-AACs is significantly lower than the curve of PC concrete in the American standard, which emphasizes the necessity of establishing the mechanical properties relationship of BFS/FA-AACs itself. Based on the fitting result, the flexural strength of BFS/FA-AACs can be predicted by Eq. (21). The standard error is 0.03 and the R^2 value is 0.35.

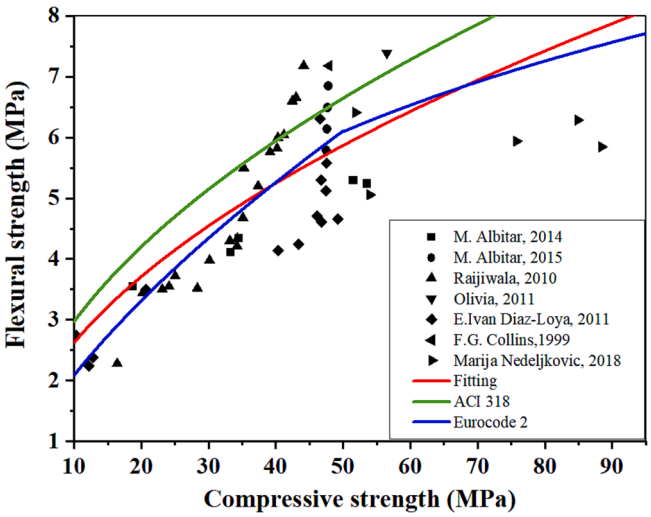

Fig. 11. Relationship between flexural strength and compressive strength of BFS/FA-AACs.

$$f_r = 0.83\sqrt{f_c'}\ (\tag{21}$$

$$f_r = 0.94\sqrt{f_c'} \tag{22}$$

$$f_r = 0.45 f_c'^{\frac{2}{3}}, f_c' \leqslant 50\ MPa \tag{23}$$

$$f_r = 3.18\ln(1 + (f_c' + 8)/10), f_c' > 50\ \text{MPa} \tag{24}$$

In which: f_r is the flexural strength of BFS/FA-AACs (MPa),f_c' is the compressive strength of BFS/FA-AACs (MPa).

3.2.3. Elastic modulus

The connection between elastic modulus and compressive strength collected from the existing literature on BFS/FA-AACs is illustrated in Fig. 12 [6,7,33,76,77,79–82,85,89–102]. According to the results, the elastic modulus (E) and the compressive strength of BFS/FA-AACs are positively correlated despite some fluctuations. The discreteness is mainly due to the aggregate difference in the data. It is discovered that aggregates have a more substantial effect on the elastic modulus of concrete than on the compressive strength of concrete [103]. Compared

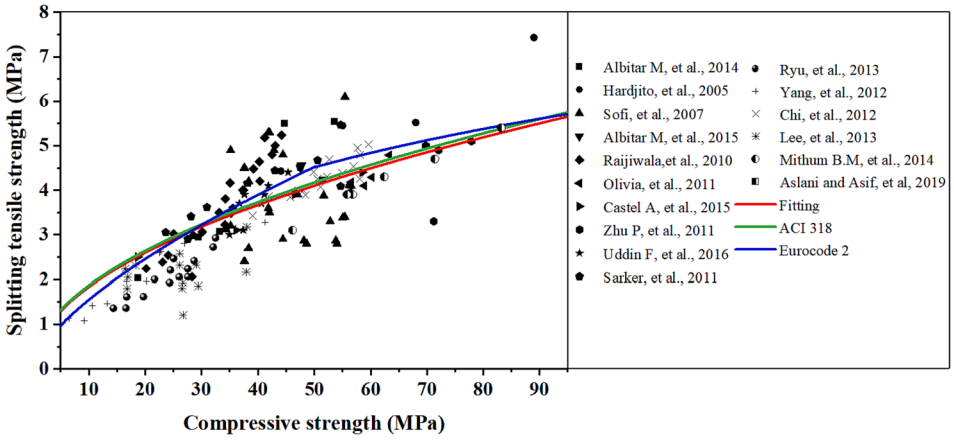

Fig. 10. Relationship between splitting tensile strength and compressive strength of BFS/FA-AACs.

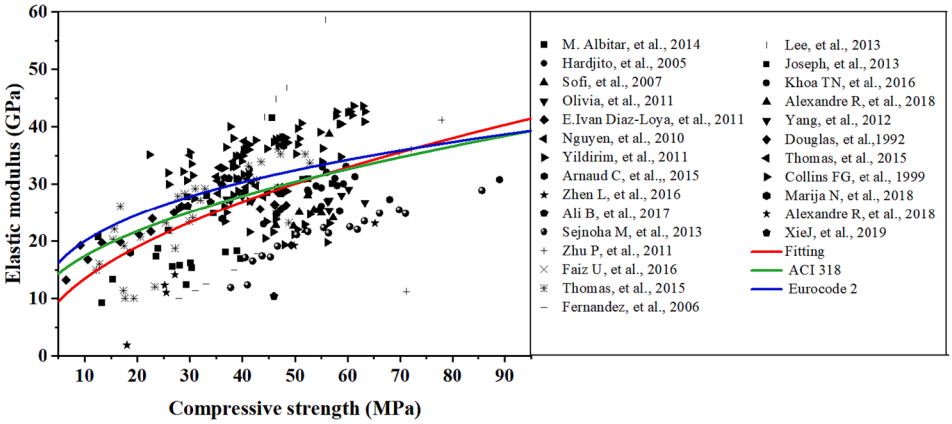

Fig. 12. Relationship between elastic modulus and compressive strength of BFS/FA-AACs.

with the other mechanical properties, the elastic modulus of concrete depends on the stiffness of paste, aggregate, and their interfacial properties. The pronounced influence of aggregate types on the elastic modulus of concrete has been detected [104–106]. In general, the elastic modulus of concrete increases with higher stiffness aggregate [107]. Nevertheless, the fitted trend of BFS/FA-AACs resembles the trend of PC concrete in the ACI standard (see Eq. (26)) and the Eurocode (see Eq. (27)). The elastic modulus of BFS/FA-AACs can be predicted by Eq. (25). The standard error is 0.07 and the R^2 value is 0.22.

$$E = 4.25\sqrt{f_c'} \tag{25}$$

$$E = 3.32\sqrt{f_c'} + 6.9 \tag{26}$$

$$E = 20\left(\frac{f_c'}{10}\right)^{0.3} \tag{27}$$

In which: E is the elastic modulus of BFS/FA-AACs (GPa), f_c' is the compressive strength of BFS/FA-AACs (MPa).

3.2.4. Poisson's ratio

The relationship between Poisson's ratio and the compressive strength of BFS/FA-AACs is demonstrated in Fig. 13 [76,77,81,89,91,92,94,102]. It is observed that Poisson's ratio (v) of BFS/FA-AACs is identical to Poisson's ratio of PC concrete, which is approximately 0.2. It reflects that Poisson's ratio of BFS/FA-AACs has little relationship with its mix design.

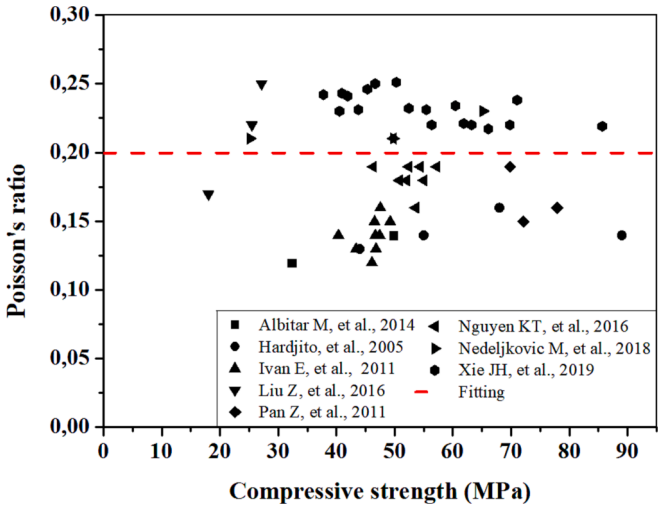

Fig. 13. Relationship between Poisson's ratio and compressive strength of BFS/FA-AACs.

4. Conclusions

In this paper, the compressive strength predictive model of BFS/FA-AAMs was established by machine learning, and the other mechanical properties predictive formulas of BFS/FA-AACs were derived by data fitting. In general, the compressive strength of BFS/FA-AAM above 7 d can be predicted with high accuracy by the GBRT model and other mechanical properties can be evaluated by the proposed formulas.The following conclusions can be drawn from the results presented:

1) The compressive strength of BFS/FA-AACs is strongly related to the model parameters, each of which contributes to a different degree. The influencing rank of the 5 parameters is BFS/b ratio > Curing time > Na_2O/b ratio > SiO_2/Na_2O ratio > w/b ratio.
2) All four machine learning methods are generally able to predict the compressive strength of BFS/FA-AAMs. Among them, GBRT and AAN show the best performance, with R^2 above 0.90. The effective rank of the 5 machine learning predictive models is GBRT > ANN > RF > RT
3) The compressive strength of BFS/FA-AACs above 7 d can be predicted with good accuracy using the GBRT model.
4) The elastic modulus, flexural strength, and splitting tensile strength of the BFS/FA-AACs are closely related to the compressive strength of the BFS/FA-AACs and can be calculated using the predicted formulas given in this paper. BFS/FA-AACs have a similar Poisson's ratio to PC concrete, which is approximately 0.2.
5) More data are required in future studies in order to modify the predictive model and formulas. In addition, when evaluating the elastic modulus of BFS/FA-AAC, special attention should be paid to the type and content of aggregates.

CRediT authorship contribution statement

Beibei SUN: Writing – review & editing, Writing – original draft, Methodology, Investigation, Formal analysis, Data curation, Conceptualization. **Luchuan DING:** Methodology, Investigation, Data curation. **Guang YE:** Supervision. **Geert De SCHUTTER:** Supervision.

Declaration of Competing Interest

The authors declare that they have no known competing financial interests or personal relationships that could have appeared to influence the work reported in this paper.

Data availability

Data will be made available on request.

Acknowledgments

This work was supported by the China Scholarship Council (Grant number. 201806370216), the Natural Science Foundation of China (Grant number. 52308197), and the China Postdoctoral Science Foundation (Grant number. 2022 M722427).

References

[1] G. Habert, J.D.E. De Lacaillerie, N. Roussel, An environmental evaluation of geopolymer based concrete production: reviewing current research trends, J. Clean. Prod. 19 (11) (2011) 1229–1238, https://doi.org/10.1016/j.jclepro.2011.03.012.
[2] L.K. Turner, F.G. Collins, Carbon dioxide equivalent (CO2-e) emissions: A comparison between geopolymer and OPC cement concrete, Constr. Build. Mater. 43 (2013) 125–130, https://doi.org/10.1016/j.conbuildmat.2013.01.023.
[3] J.S. van Deventer, J.L. Provis, P. Duxson, D.G. Brice, Chemical research and climate change as drivers in the commercial adoption of alkali activated materials, Waste Biomass Valoriz. 1 (1) (2010) 145–155, https://doi.org/10.1007/s12649-010-9015-9.
[4] K. Arbi, M. Nedeljkovic, Y. Zuo, S. Grünewald, A. Keulen, G. Ye, Experimental Study on the Workability of Alkali Activated Fly Ash and Slag-Based Geopolymer Concrete (2015) 75–78.
[5] M. Nedeljković, Y. Zuo, K. Arbi, G. Ye, Carbonation resistance of alkali-activated slag under natural and accelerated conditions, Journal of Sustainable Metallurgy 4 (1) (2018) 33–49, https://doi.org/10.1007/s40831-018-0166-4.
[6] A.M. Fernandez-Jimenez, A. Palomo, C. Lopez-Hombrados, Engineering properties of alkali-activated fly ash concrete, ACI Mater. J. 103 (2) (2006) 106. https://doi.org/10.14359/15261.
[7] M. Sofi, J. Van Deventer, P. Mendis, G. Lukey, Engineering properties of inorganic polymer concretes (IPCs), Cem. Concr. Res. 37 (2) (2007) 251–257, https://doi.org/10.1016/j.cemconres.2006.10.008.
[8] A.M. Rashad, A comprehensive overview about the influence of different additives on the properties of alkali-activated slag–A guide for Civil Engineer, Constr. Build. Mater. 47 (2013) 29–55, https://doi.org/10.1016/j.conbuildmat.2013.04.011.
[9] M.O. Yusuf, M.A.M. Johari, Z.A. Ahmad, M.J.M. Maslehuddin, Evolution of alkaline activated ground blast furnace slag–ultrafine palm oil fuel ash based concrete, Materials Design 55 (2014) 387–393, https://doi.org/10.1016/j.matdes.2013.09.047.
[10] M. Nedeljkovic, Z. Li, G. Ye, Setting, Strength, and Autogenous Shrinkage of Alkali-Activated Fly Ash and Slag Pastes: Effect of Slag Content, Materials (Basel, Switzerland) 11 (11) (2018), https://doi.org/10.3390/ma11112121.
[11] M. Ibrahim, M. Maslehuddin, An overview of factors influencing the properties of alkali-activated binders, J. Clean. Prod. 286 (2021), 124972, https://doi.org/10.1016/j.jclepro.2020.124972.
[12] R. Mohamed, R. Abd Razak, M.M.A.B. Abdullah, S.Z. Abd Abd Rahim, L. Yuan-Li, A.V. Sandu, J.J. Wysłocki, Heat evolution of alkali-activated materials: A review on influence factors, Construction and Building Materials 314 (2022), 125651, https://doi.org/10.1016/j.conbuildmat.2021.125651.
[13] X. Ouyang, Y. Ma, Z. Liu, J. Liang, G. Ye, Effect of the sodium silicate modulus and slag content on fresh and hardened properties of alkali-activated fly ash/slag, Minerals 10 (1) (2020) 15, https://doi.org/10.3390/min10010015.
[14] K.K. Ramagiri, D.R. Chauhan, S. Gupta, A. Kar, D. Adak, A. Mukherjee, High-temperature performance of ambient-cured alkali-activated binder concrete, Innovative Infrastructure, Solutions 6 (2) (2021), https://doi.org/10.1007/s41062-020-00448-y.
[15] G.F. Huseien, A.R.M. Sam, R. Alyousef, Texture, morphology and strength performance of self-compacting alkali-activated concrete: Role of fly ash as GBFS replacement, Constr. Build. Mater. 270 (2021), https://doi.org/10.1016/j.conbuildmat.2020.121368.
[16] M.H. Rafiei, W.H. Khushefati, R. Demirboga, H. Adeli, Supervised Deep Restricted Boltzmann Machine for Estimation of Concrete, ACI Mater. J. 114 (2) (2017). https://doi.org/10.14359/51689560.
[17] M. Kuhn, K. Johnson, Applied predictive modeling, Springer (2013), https://doi.org/10.1007/978-1-4614-6849-3.
[18] U. Atici, Prediction of the strength of mineral admixture concrete using multivariable regression analysis and an artificial neural network, Expert Syst. Appl. 38 (8) (2011) 9609–9618, https://doi.org/10.1016/j.eswa.2011.01.156.
[19] S. Saad, M. Ishtiyaque, H. Malik, Selection of most relevant input parameters using WEKA for artificial neural network based concrete compressive strength prediction model, IEEE 7th Power India International Conference (PIICON), IEEE 2016 (2016) 1–6, https://doi.org/10.1109/poweri.2016.8077368.
[20] I.B. Topcu, M. Sarıdemir, Prediction of compressive strength of concrete containing fly ash using artificial neural networks and fuzzy logic, Comput. Mater. Sci 41 (3) (2008) 305–311, https://doi.org/10.1016/j.commatsci.2007.04.009.
[21] I. Yeh, Modeling of strength of high-performance concrete using artificial neural networks, Cem. Concr. Res. 28 (12) (1998) 1797–1808, https://doi.org/10.1016/s0008-8846(98)00165-3.
[22] Q. Han, C. Gui, J. Xu, G. Lacidogna, A generalized method to predict the compressive strength of high-performance concrete by improved random forest algorithm, Constr. Build. Mater. 226 (2019) 734–742, https://doi.org/10.1016/j.conbuildmat.2019.07.315.
[23] A. Nazari, F. Torgal, Predicting compressive strength of different geopolymers by artificial neural networks, Ceram. Int. 39 (3) (2013) 2247–2257, https://doi.org/10.1016/j.ceramint.2012.08.070.
[24] K.T. Nguyen, Q.D. Nguyen, T.A. Le, J. Shin, K. Lee, Analyzing the compressive strength of green fly ash based geopolymer concrete using experiment and machine learning approaches, Constr. Build. Mater. 247 (2020), 118581, https://doi.org/10.1016/j.conbuildmat.2020.118581.
[25] E. Gomaa, T. Han, M. ElGawady, J. Huang, A. Kumar, Machine learning to predict properties of fresh and hardened alkali-activated concrete, Cem. Concr. Compos. 115 (2021), 103863, https://doi.org/10.1016/j.cemconcomp.2020.103863.
[26] B. Sun, G. Ye, G. De Schutter, A review: Reaction mechanism and strength of slag and fly ash-based alkali-activated materials, Constr. Build. Mater. 326 (2022), 126843, https://doi.org/10.1016/j.conbuildmat.2022.126843.
[27] B. Sun, Y. Sun, G. Ye, G. De Schutter, A mix design methodology of slag and fly ash-based alkali-activated paste, Cem. Concr. Compos. 126 (2022), https://doi.org/10.1016/j.cemconcomp.2021.104368.
[28] B. Sun, Y. Sun, G. Ye, G. De Schutter, A mix design methodology of blast furnace slag and fly ash-based alkali-activated concrete, Cem. Concr. Compos. (2023), 105076, https://doi.org/10.1016/j.cemconcomp.2023.105076.
[29] A. Rafeet, R. Vinai, M. Soutsos, W. Sha, Guidelines for mix proportioning of fly ash/GGBS based alkali activated concretes, Constr. Build. Mater. 147 (2017) 130–142, https://doi.org/10.1016/j.conbuildmat.2017.04.036.
[30] M.S. Reddy, P. Dinakar, B. Rao, Mix design development of fly ash and ground granulated blast furnace slag based geopolymer concrete, Journal of Building, Engineering 20 (2018) 712–722, https://doi.org/10.1016/j.jobe.2018.09.010.
[31] G. Fang, W.K. Ho, W. Tu, M. Zhang, Workability and mechanical properties of alkali-activated fly ash-slag concrete cured at ambient temperature, Constr. Build. Mater. 172 (2018) 476–487, https://doi.org/10.1016/j.conbuildmat.2018.04.008.
[32] P.S. Deb, P. Nath, P.K. Sarker, The effects of ground granulated blast-furnace slag blending with fly ash and activator content on the workability and strength properties of geopolymer concrete cured at ambient temperature, Materials & Design (1980-2015) 62 (2014) 32-39. https://doi.org/10.1016/j.matdes.2014.05.001.
[33] N.K. Lee, H.K. Lee, Setting and mechanical properties of alkali-activated fly ash/slag concrete manufactured at room temperature, Constr. Build. Mater. 47 (2013) 1201–1209, https://doi.org/10.1016/j.conbuildmat.2013.05.107.
[34] P. Nath, P.K. Sarker, Effect of GGBFS on setting, workability and early strength properties of fly ash geopolymer concrete cured in ambient condition, Constr. Build. Mater. 66 (2014) 163–171, https://doi.org/10.1016/j.conbuildmat.2014.05.080.
[35] K. Vijai, R. Kumutha, B. Vishnuram, Effect of types of curing on strength of geopolymer concrete, International Journal of Physical Sciences 5 (9) (2010) 1419–1423.
[36] Y. Ding, Experimental study on fracture properties of alkali-activated concrete, (2017).
[37] F. Shahrajabian, K. Behfarnia, The effects of nano particles on freeze and thaw resistance of alkali-activated slag concrete, Constr. Build. Mater. 176 (2018) 172–178, https://doi.org/10.1016/j.conbuildmat.2018.05.033.
[38] T. Xie, T. Ozbakkaloglu, Behavior of low-calcium fly and bottom ash-based geopolymer concrete cured at ambient temperature, Ceram. Int. 41 (4) (2015) 5945–5958, https://doi.org/10.1016/j.ceramint.2015.01.031.
[39] A.M. Humad, A. Kothari, J.L. Provis, A. Cwirzen, The effect of blast furnace slag/fly ash ratio on setting, strength, and shrinkage of alkali-activated pastes and concretes, Front. Mater. 6 (2019) 9, https://doi.org/10.3389/fmats.2019.00009.
[40] N.A. Farhan, M.N. Sheikh, M.N.S. Hadi, Investigation of engineering properties of normal and high strength fly ash based geopolymer and alkali-activated slag concrete compared to ordinary Portland cement concrete, Constr. Build. Mater. 196 (2019) 26–42, https://doi.org/10.1016/j.conbuildmat.2018.11.083.
[41] A. Kothari, Effects of Fly Ash on the properties of Alkali Activated Slag Concrete, 2017.
[42] B. Mithun, M. Narasimhan, Self-cured alkali activated slag concrete mixes-an experimental study, International Journal of Civil Environmental Engineering 8 (4) (2014) 477–482.
[43] K. Orosz, A. Humad, H. Hedlund, A. Cwirzen, Autogenous Deformation of Alkali-Activated Blast Furnace Slag Concrete Subjected to Variable Curing Temperatures, Advances in Civil Engineering 2019 (2019) 1–8, https://doi.org/10.1155/2019/6903725.
[44] F. Aslani, Z. Asif, Properties of Ambient-Cured Normal and Heavyweight Geopolymer Concrete Exposed to High Temperatures, Materials 12 (2019), https://doi.org/10.3390/ma12050740.
[45] F. Puertas, B. González-Fonteboa, I. González-Taboada, M. Alonso, M. Torres-Carrasco, G. Rojo, F.J.C. Martínez-Abella, C. Composites, Alkali-Activated Slag Concrete: Fresh and Hardened Behaviour 85 (2018) 22–31, https://doi.org/10.1016/j.cemconcomp.2017.10.003.
[46] C.S. Thunuguntla, T.D. Gunneswara Rao, Mix Design Procedure for Alkali-Activated Slag Concrete Using Particle Packing Theory, J. Mater. Civ. Eng. 30 (6) (2018), https://doi.org/10.1061/(asce)mt.1943-5533.0002296.

[47] D. Bondar, S.V. Nanukuttan, M.N. Soutsos, P.M. Basheer, J.L. Provis, Suitability of alkali activated GGBS/Fly ash concrete for chloride environments, ACI Special Publications, American Concrete Institute, 2017, pp. 35.1-35.14. https://doi.org/10.14359/51701073.

[48] D. Bondar, S. Nanukuttan, J.L. Provis, M. Soutsos, Efficient mix design of alkali activated slag concretes based on packing fraction of ingredients and paste thickness, J. Clean. Prod. 218 (2019) 438–449, https://doi.org/10.1016/j.jclepro.2019.01.332.

[49] P.S. Deb, P. Nath, P. Sarker, The effects of ground granulated blast-furnace slag blending with fly ash and activator content on the workability and strength properties of geopolymer concrete cured at ambient temperature, Mater. Des. 62 (2014) 32–39, https://doi.org/10.1016/j.matdes.2014.05.001.

[50] Z. Zhang, L. Li, X. Ma, H. Wang, Compositional, microstructural and mechanical properties of ambient condition cured alkali-activated cement, Constr. Build. Mater. 113 (2016) 237–245, https://doi.org/10.1016/j.conbuildmat.2016.03.043.

[51] X. Gao, Q.L. Yu, H.J.H. Brouwers, Reaction kinetics, gel character and strength of ambient temperature cured alkali activated slag–fly ash blends, Constr. Build. Mater. 80 (2015) 105–115, https://doi.org/10.1016/j.conbuildmat.2015.01.065.

[52] G. Fang, Q. Wang, M. Zhang, Micromechanical analysis of interfacial transition zone in alkali-activated fly ash-slag concrete, Cem. Concr. Compos. 119 (2021), 103990, https://doi.org/10.1016/j.cemconcomp.2021.103990.

[53] G. Fang, M. Zhang, The evolution of interfacial transition zone in alkali-activated fly ash-slag concrete, Cem. Concr. Res. 129 (2020), 105963, https://doi.org/10.1016/j.cemconres.2019.105963.

[54] Z. Luo, W. Li, K. Wang, A. Castel, S.P. Shah, Comparison on the properties of ITZs in fly ash-based geopolymer and Portland cement concretes with equivalent flowability, Cem. Concr. Res. 143 (2021), 106392, https://doi.org/10.1016/j.cemconres.2021.106392.

[55] W. Lee, J. Van Deventer, The interface between natural siliceous aggregates and geopolymers, Cem. Concr. Res. 34 (2) (2004) 195–206, https://doi.org/10.1016/S0008-8846(03)00250-3.

[56] A. Brough, A. Atkinson, Automated identification of the aggregate–paste interfacial transition zone in mortars of silica sand with Portland or alkali-activated slag cement paste, Cem. Concr. Res. 30 (6) (2000) 849–854, https://doi.org/10.1016/S0008-8846(00)00254-4.

[57] R. San Nicolas, J.L. Provis, The interfacial transition zone in alkali-activated slag mortars, Front. Mater. 2 (2015) 70, https://doi.org/10.3389/fmats.2015.00070.

[58] R. San Nicolas, S.A. Bernal, R.M. de Gutiérrez, J.S. van Deventer, J.L. Provis, Distinctive microstructural features of aged sodium silicate-activated slag concretes, Cem. Concr. Res. 65 (2014) 41–51, https://doi.org/10.1016/j.cemconres.2014.07.008.

[59] B. Fu, D.C. Feng, A machine learning-based time-dependent shear strength model for corroded reinforced concrete beams, Journal of Building Engineering 36 (2021), 102118, https://doi.org/10.1016/j.jobe.2020.102118.

[60] Q. Ren, L. Ding, X. Dai, Z. Jiang, G. De Schutter, Prediction of Compressive Strength of Concrete with Manufactured Sand by Ensemble Classification and Regression Tree Method, J. Mater. Civ. Eng. 33 (7) (2021) 04021135, https://doi.org/10.1061/(asce)mt.1943-5533.0003741.

[61] G. Ridgeway, Generalized Boosted Models: A guide to the gbm package, Update 1 (1) (2007) 2007.

[62] J.H. Friedman, Greedy function approximation: a gradient boosting machine, Ann. Stat. (2001) 1189–1232, https://doi.org/10.1214/aos/1013203451.

[63] T. Fawcett, Using rule sets to maximize ROC performance, IEEE (2001) 131–138, https://doi.org/10.1109/icdm.2001.989510.

[64] F. Pedregosa, G. Varoquaux, A. Gramfort, V. Michel, B. Thirion, O. Grisel, M. Blondel, P. Prettenhofer, R. Weiss, V. Dubourg, Scikit-learn: Machine learning in Python, The Journal of Machine Learning Research 12 (2011) 2825–2830.

[65] D.C. Feng, Z.T. Liu, X.D. Wang, Z.M. Jiang, S.X. Liang, Failure mode classification and bearing capacity prediction for reinforced concrete columns based on ensemble machine learning algorithm, Adv. Eng. Inf. 45 (2020), 101126, https://doi.org/10.1016/j.aei.2020.101126.

[66] L. Breiman, Random forests, Mach. Learn. 45 (1) (2001) 5–32.

[67] J. Zhang, D. Li, Y. Wang, Toward intelligent construction: prediction of mechanical properties of manufactured-sand concrete using tree-based models, J. Clean. Prod. 258 (2020), 120665, https://doi.org/10.1016/j.jclepro.2020.120665.

[68] D.C. Feng, W.J. Wang, S. Mangalathu, G. Hu, T. Wu, Implementing ensemble learning methods to predict the shear strength of RC deep beams with/without web reinforcements, Eng. Struct. 235 (2021), 111979, https://doi.org/10.1016/j.engstruct.2021.111979.

[69] R.A. Berk, Statistical learning from a regression perspective, Springer, 2008.

[70] W.Y. Loh, Classification and regression trees, Wiley Interdisciplinary Reviews, Data Min. Knowl. Disc. 1 (1) (2011) 14–23, https://doi.org/10.1002/widm.8.

[71] T.W. Kim, J.B. Valdés, Nonlinear model for drought forecasting based on a conjunction of wavelet transforms and neural networks, J. Hydrol. Eng. 8 (6) (2003) 319–328, https://doi.org/10.1061/(asce)1084-0699(2003)8:6(319).

[72] B. Ghorbani, A. Arulrajah, G. Narsilio, S. Horpibulsuk, Experimental investigation and modelling the deformation properties of demolition wastes subjected to freeze–thaw cycles using ANN and SVR, Constr. Build. Mater. 258 (2020), 119688, https://doi.org/10.1016/j.conbuildmat.2020.119688.

[73] B. Kim, Y.H. Park, Beginner's guide to neural networks for the MNIST dataset using MATLAB, The Korean Journal of Mathematics 26 (2) (2018) 337–348. https://doi.org/10.11568/kjm.2018.26.2.337.

[74] T.M. Matlab, R 2019b The MathWorks, Inc (2019).

[75] M. Albitar, P. Visintin, M. Ali, Engineering properties of Class-F fly ash-based geopolymer concrete, Construction Materials and Structures (2014) 495–502, https://doi.org/10.3233/978-1-61499-466-4-495.

[76] D. Hardjito, B.V. Rangan, Development and properties of low-calcium fly ash-based geopolymer concrete, (2005).

[77] M. Albitar, P. Visintin, M.S. Mohamed Ali, M. Drechsler, Assessing behaviour of fresh and hardened geopolymer concrete mixed with class-F fly ash, KSCE J. Civ. Eng. 19 (5) (2014) 1445–1455, https://doi.org/10.1007/s12205-014-1254-z.

[78] D. Raijiwala, H. Patil, Geopolymer concrete A green concrete, 2010 2nd international conference on Chemical, Biological and Environmental Engineering, IEEE, 2010, pp. 202-206. https://doi.org/10.1109/icbee.2010.5649609.

[79] M. Olivia, Durability related properties of low calcium fly ash based geopolymer concrete, Curtin University, 2011.

[80] A. Castel, S.J. Foster, Bond strength between blended slag and Class F fly ash geopolymer concrete with steel reinforcement, Cem. Concr. Res. 72 (2015) 48–53, https://doi.org/10.1016/j.cemconres.2015.02.016.

[81] Z. Pan, J.G. Sanjayan, B.V. Rangan, Fracture properties of geopolymer paste and concrete, Mag. Concr. Res. 63 (10) (2011) 763–771, https://doi.org/10.1680/macr.2011.63.10.763.

[82] F.U.A. Shaikh, Mechanical and durability properties of fly ash geopolymer concrete containing recycled coarse aggregates, Int. J. Sustain. Built Environ. 5 (2) (2016) 277–287, https://doi.org/10.1016/j.ijsbe.2016.05.009.

[83] P.K. Sarker, Bond strength of reinforcing steel embedded in fly ash-based geopolymer concrete, Materials Structures 44 (5) (2011) 1021–1030, https://doi.org/10.1617/s11527-010-9683-8.

[84] G.S. Ryu, Y.B. Lee, K.T. Koh, Y.S. Chung, The mechanical properties of fly ash-based geopolymer concrete with alkaline activators, Constr. Build. Mater. 47 (2013) 409–418, https://doi.org/10.1016/j.conbuildmat.2013.05.069.

[85] K.H. Yang, A.R. Cho, J. Song, Effect of water–binder ratio on the mechanical properties of calcium hydroxide-based alkali-activated slag concrete, Constr. Build. Mater. 29 (2012) 504–511, https://doi.org/10.1016/j.conbuildmat.2011.10.062.

[86] M. Chi, Effects of dosage of alkali-activated solution and curing conditions on the properties and durability of alkali-activated slag concrete, Constr. Build. Mater. 35 (2012) 240–245, https://doi.org/10.1016/j.conbuildmat.2012.04.005.

[87] A. Committee, Building code requirements for structural concrete (ACI 318–08) and commentary, American Concrete Institute, 2008.

[88] B. En, 1–2: 2004 Eurocode 2: Design of concrete structures-Part 1–2: General rules-Structural fire design, European Standards, London, 2004.

[89] E.I. Diaz-Loya, E.N. Allouche, S.J. Vaidya, Mechanical properties of fly-ash-based geopolymer concrete, ACI Mater. J. 108 (3) (2011) 300. https://doi.org/10.14359/51682495.

[90] F. Collins, J.G. Sanjayan, Workability and mechanical properties of alkali activated slag concrete, Cem. Concr. Res. 29 (3) (1999) 455–458, https://doi.org/10.1016/s0008-8846(98)00236-1.

[91] M. Nedeljković, Carbonation mechanism of alkali-activated fly ash and slag materials: In view of long-term performance predictions, 2019.

[92] K.T. Nguyen, N. Ahn, T.A. Le, K. Lee, Theoretical and experimental study on mechanical properties and flexural strength of fly ash-geopolymer concrete, Constr. Build. Mater. 106 (2016) 65–77, https://doi.org/10.1016/j.conbuildmat.2015.12.033.

[93] H. Yildirim, M. Sümer, V. Akyüncü, E. Gürbüz, Comparison on efficiency factors of F and C types of fly ashes, Constr. Build. Mater. 25 (6) (2011) 2939–2947, https://doi.org/10.1016/j.conbuildmat.2010.12.009.

[94] Z. Liu, C.S. Cai, H. Peng, F. Fan, Experimental Study of the Geopolymeric Recycled Aggregate Concrete, J. Mater. Civ. Eng. 28 (9) (2016), https://doi.org/10.1061/(asce)mt.1943-5533.0001584.

[95] A. Bagheri, A. Nazari, J.G. Sanjayan, P. Rajeev, W. Duan, Fly ash-based boroaluminosilicate geopolymers: Experimental and molecular simulations, Ceram. Int. 43 (5) (2017) 4119–4126, https://doi.org/10.1016/j.ceramint.2016.12.020.

[96] M. Šejnoha, M. Brouček, E. Novotná, Z. Keršner, D. Lehký, P. Frantík, Fracture properties of cement and alkali activated fly ash based concrete with application to segmental tunnel lining, Adv. Eng. Softw. 62–63 (2013) 61–71, https://doi.org/10.1016/j.advengsoft.2013.04.009.

[97] R.J. Thomas, S. Peethamparan, Alkali-activated concrete: Engineering properties and stress–strain behavior, Constr. Build. Mater. 93 (2015) 49–56, https://doi.org/10.1016/j.conbuildmat.2015.04.039.

[98] B. Joseph, G. Mathew, Influence of aggregate content on the behavior of fly ash based geopolymer concrete, Sci. Iran. 19 (5) (2012) 1188–1194, https://doi.org/10.1016/j.scient.2012.07.006.

[99] J.R. Yost, A. Radlińska, S. Ernst, M. Salera, Structural behavior of alkali activated fly ash concrete. Part 1: mixture design, material properties and sample fabrication, Mater. Struct. 46 (3) (2013) 435–447, https://doi.org/10.1617/s11527-012-9919-x.

[100] A. Rodrigue, J. Duchesne, B. Fournier, B. Bissonnette, Influence of added water and fly ash content on the characteristics, properties and early-age cracking sensitivity of alkali-activated slag/fly ash concrete cured at ambient temperature, Constr. Build. Mater. 171 (2018) 929–941, https://doi.org/10.1016/j.conbuildmat.2018.03.176.

[101] E. Douglas, A. Bilodeau, V. Malhotra, Properties and durability of alkali-activated slag concrete, Materials Journal 89 (5) (1992) 509–516. https://doi.org/10.14359/1832.

[102] J. Xie, J. Wang, B. Zhang, C. Fang, L. Li, Physicochemical properties of alkali activated GGBS and fly ash geopolymeric recycled concrete, Constr. Build. Mater. 204 (2019) 384–398, https://doi.org/10.1016/j.conbuildmat.2019.01.191.

[103] P.K. Mehta, P.J. Monteiro, Concrete: microstructure, properties, and materials, McGraw-Hill Education, 2014.
[104] S. Ahmad, S.A. Alghamdi, A study on effect of coarse aggregate type on concrete performance, Arab. J. Sci. Eng. 37 (2012) 1777–1786, https://doi.org/10.1007/s13369-012-0282-6.
[105] M. Alexander, S. Mindess, Aggregates in concrete, CRC Press (2005), https://doi.org/10.1201/9781482264647.
[106] M. Rashid, M. Mansur, P. Paramasivam, Correlations between mechanical properties of high-strength concrete, J. Mater. Civ. Eng. 14 (3) (2002) 230–238, https://doi.org/10.1061/(asce)0899-1561(2002)14:3(230).
[107] M. Uysal, The influence of coarse aggregate type on mechanical properties of fly ash additive self-compacting concrete, Constr. Build. Mater. 37 (2012) 533–540, https://doi.org/10.1016/j.conbuildmat.2012.07.085.